Acta Materialia 216 (2021) 117135

Contents lists available at ScienceDirect

Acta Materialia

journal homepage: www.elsevier.com/locate/actamat

Full length article

Element-resolved local lattice distortion in complex concentrated alloys: An observable signature of electronic effects

Hyun Seok Oh[a,b], Khorgolkhuu Odbadrakh[c], Yuji Ikeda[d,e], Sai Mu[f], Fritz Körmann[d,g], Cheng-Jun Sun[h], Heh Sang Ahn[a], Kook Noh Yoon[a], Duancheng Ma[i], Cemal Cem Tasan[b,*], Takeshi Egami[f,k,*], Eun Soo Park[a,*]

[a] Department of Materials Science and Engineering, Seoul National University, Seoul 08826, Republic of Korea
[b] Department of Materials Science and Engineering, Massachusetts Institute of Technology, MA 02139, USA
[c] Joint Institute for Computational Sciences, University of Tennessee and Oak Ridge National Laboratory, Oak Ridge, TN 37996, USA
[d] Max-Planck-Institut für Eisenforschung, Max-Planck-Straße 1, 40237 Düsseldorf, Germany
[e] Institute for Materials Science, University of Stuttgart, Pfaffenwaldring 55, 70569 Stuttgart, Germany
[f] Materials Science and Technology Division, Oak Ridge National Laboratory, Oak Ridge, TN 37831, USA
[g] Materials Science and Engineering, Delft University of Technology, 2628 CD Delft, Netherlands
[h] Advanced Photon Source, Argonne National Laboratory, Argonne, IL 60439 USA
[i] Department of Materials Science and Engineering, Friedrich-Alexander-Universität, 91054 Erlangen, Germany
[k] Department of Materials Science and Engineering and Department of Physics and Astronomy, University of Tennessee, Knoxville, TN 37996, USA

ARTICLE INFO

Article history:
Received 7 January 2021
Revised 17 June 2021
Accepted 25 June 2021
Available online 1 July 2021

Keywords:
Complex concentrated alloy
Element-resolved local lattice distortion
Charge transfer
Magnetism
Short-range order

ABSTRACT

Complex concentrated alloys (CCAs) are of growing interest due to their outstanding mechanical properties that exceed the property limits of conventional alloys. Whereas the superior properties are often attributed to severe lattice distortion, to date it is not clear what controls the lattice distortion and how it affects the mechanical properties of CCAs. In this work, we study the element-resolved local lattice distortion (ELLD) in CCAs of 3d transition-metal elements (3d CCAs) by the extended X-ray absorption fine structure experiment and the density-functional theory calculations. We show that ELLD is primarily dependent upon charge transfer among elements and affects the properties through atomic-level pressure and orbital transition. The ELLD provides a qualitative measure of the effective atomic size for explaining element-specific properties and macroscopic properties.

1. Introduction

Complex concentrated alloys (CCAs) including high-entropy alloys (HEAs) are composed of multiple principal elements, and the interplay among constituent elements determines the overall properties [1]. Because they are chemically complex, it is challenging to elucidate their properties in terms of detailed features of local atomic structure in CCAs. For example, severe lattice distortion (**Fig. S1**) has been suggested to be responsible for various desirable properties [1,2], such as solid-solution strengthening [3–5], sluggish diffusion [6], unusual electrical and thermal conductivity [7,8], and irradiation resistance [7,9]. A number of experimental [4,5,10–14], computational [3–5,14–19], and theoretical studies [20,21] have addressed the lattice distortion of CCAs and discussed its relationship with properties. However, how local lattice distortion varies with composition in CCAs remains poorly understood.

A major challenge is that we have to evaluate the electronic contributions to the local structure in order to characterize the local lattice distortion properly. In a simple binary single-phase alloy, the local atomic volume, such as the Voronoi atomic volume, and the atomic-level pressure are correlated. Large atoms occupy large volumes and are under compression, while small atoms occupy small volumes and are under tension. However, in CCAs, it is much more complex. It was recently shown that the local atomic volumes are not correlated with the atomic-level pressures in single-phase face-centered cubic (*fcc*) CCAs consisting of 3d transition-metal elements (Cr, Mn, Fe, Co, and Ni) (3d CCAs) [14]. This is because the atomic-level pressures are dominated by the local charge transfer between neighboring elements. For example, in CrMnFeCoNi CCA, Cr atoms have large Voronoi atomic volumes but have

* Corresponding author:
E-mail addresses: tasan@mit.edu (C.C. Tasan), egami@utk.edu (T. Egami), espark@snu.ac.kr (E.S. Park).

https://doi.org/10.1016/j.actamat.2021.117135

small effective atomic sizes due to charge transfer away from Cr. Consequently, they are under tension. Therefore, when we consider CCAs we have to depart from the conventional practice in order to understand the atomic structure-property correlation.

In this work we discuss how charge transfer (electronic effects) affects the lattice distortion (atomic structure) and effective atomic size (local energy landscape), resulting in controlling the properties of 3d CCAs. We demonstrate that the element-resolved local lattice distortion (ELLD), defined either by the local static fluctuation of bond lengths or by the average atomic displacement of each element, is an excellent qualitative structural signature of charge transfer and effective atomic size in 3d CCAs. First, we show that the fluctuation of bond lengths in each element, which is experimentally measured through extended X-ray absorption fine structure (EXAFS) for various equiatomic 3d CCAs, correlates well with the atomic number. Second, we investigate the physical origin of the observed correlation by performing density-functional theory (DFT) simulations. We show that charge transfer is the primary cause of the observed correlation, rather than other factors, including Voronoi atomic volume, magnetism, and chemical short-range order (CSRO). The causal relationship between the charge transfer and the properties is then interpreted in terms of the atomic-level pressure and orbital transfer, both of which are related to the effective size of each element in the alloy. This study provides a new link between the structural characteristics and properties in CCAs with their electronic origins, which will help establish the holistic processing-structure-properties-performance view for a well-targeted design of CCAs.

2. Methods

2.1. Sample preparation

CCAs studied in the present work (Ni, CoNi, FeNi, MnCoNi, MnFeNi, CrCoNi, FeCoNi, CrMnCoNi, MnFeCoNi, CrFeCoNi, CrMnFeCoNi) were produced by the arc melting method using pure elements with above 99.9% purity under Ti-gettered Argon atmosphere. The as-cast buttons were suction casted followed by homogenization, cold rolling, and recrystallization annealing, and then ground into a 15 μm-thick ribbon. Conditions are described in detail in the method section of a previous study[14].

2.2. EXAFS analysis

EXAFS measurements were carried out at the 20-BM beamline of Advanced Photon Source in Argonne National Laboratory. The X-ray absorption spectra for Cr, Mn, Fe, Co, and Ni were collected in transmission mode using 0.8 mm$\times$4 mm unfocused X-ray beam to include more than 100 grains for uniformity. A Si (111) monochromator was detuned to 70–85% of its original intensity to reject higher-order harmonics. Samples were cooled in the cryogenic chamber under vacuum condition. The obtained datasets of 3d CCAs were aligned and processed to avoid instrumental background and absorption from other edges using the Athena in the IFEFFIT 1.2.11d suite of software [22]. All processes were conducted in the same conditions: pre-edge range with the energy of -150 to -30 eV, normalization range with the energy of 50–500 eV, and spline range with wave numbers of 0–11 Å^{-1}. The extracted EXAFS data were weighted by k^2 and then converted to R space by Fourier transformation to obtain the magnitude plots of the EXAFS spectra. The first peaks of each element at different temperatures were fitted simultaneously considering the Einstein equation using the Artemis software. The theoretical calculation of the amplitude reduction factors of Cr (0.955), Mn (0.935), Fe (0.941), Co (0.947), and Ni (0.951) was performed using the FEFF8.4 code [23]. Fitting conditions are described in detail in the method section of a previous study [14].

2.3. DFT calculations

2.3.1. Impact of various factors on lattice distortion in CrMnFeCoNi

To evaluate the impact of different factors (atomic volume, charge transfer, magnetic states, and possible CSRO) on lattice distortion in CrMnFeCoNi, we conducted DFT calculations with supercell models based on special quasi-random structure (SQS) [24] construction. To optimize the atomic positions, the projected augmented wave method (PAW) [25] as implemented in Vienna ab-initio simulation package (VASP) [26,27] was utilized. The exchange-correlation was treated in the Generalized Gradient Approximation (GGA), parametrized by Perdew *et al.* [28]. The 240-atom containing supercells model constructed from a 3$\times$4$\times$5 expansion of the conventional *fcc* cubic unit cell was used. The plane wave energy cutoff of 400 eV and a Γ-centered 4$\times$3$\times$2 k-point mesh was applied. The Methfessel-Paxton scheme was used with smearing 0.1 eV. Total energies were minimized until they converged within 5×10^{-4} eV per supercell. Internal atomic positions were relaxed until forces on atoms are less than 5×10^{-2} eV/Å, while the cell shape was again kept fixed.

We considered two scenarios for elucidating the impact of magnetism. First, we performed spin-polarized ferromagnetic (FM) calculations, where Cr and Mn have antiparallel magnetic moments to Fe, Co, and Ni [29]. In addition, we employed non-spin-polarized calculations which we refer to as non-magnetic (NM). The latter is not the same as, e.g., a disordered local moment approach in which local magnetic moments still persist (paramagnetic). Note that, in supercell-model calculations for CrMnFeCoNi-based CCAs, the magnetic moments of Cr and Mn initialized as described above tend to be aligned locally antiferromagnetically [30–32], and also that recently *ab initio* calculations predict an antiferromagnetic phase for CrMnFeCoNi-based CCAs, where e.g., Mn and Fe have layered antiferromagnetic alignments [33,34]. We also considered the fully disordered A1 phase and a partly disordered $L1_2$ phase where Cr occupies only one of four *fcc* sublattices. Both the A1 and the $L1_2$ phases were modeled based on the concept of SQS introduced above. For better energy convergence we calculated 10 different SQSs for each magnetic phase.

To further corroborate our findings, we performed additional atomic charge calculations for these configurations based on the Bader analysis [35] as implemented by Henkelman et al. [36] We computed the Bader charges on atoms for two configurations for each phase.

2.3.2. Atomic-level pressure and charge transfer in 3d CCAs

To evaluate the atomic-level pressure, we conducted further DFT calculations with supercell models using the VASP code mentioned above based on the same methodology. The 256-supercell models were obtained based on SQS configurations. Cutoff energy and smearing parameters for the Methfessel-Paxton scheme were chosen as above. The Γ-centered 2$\times$2$\times$2 Monkhorst-Pack grids [37] for the Brillouin zone integration were used. The equilibrium volumes of the SQS structures were first optimized until the pressure vanishes, followed by atomic relaxation until the Hellmann-Feynman forces were lower than 0.005 eV/Å. The cubic cell shape was kept throughout our calculations. All supercell calculations, except for CrCoNi, were performed based on collinear magnetic states[1].

[1] CrCoNi is treated as nonmagnetic considering a previous publication [62], which shows that the measured magnetization of CrCoNi is 0.004 μ_B/atom even in the presence of H=5T. Although not included in this paper, we also checked magnetic CrCoNi (collinear), and the displacement pattern was more or less inert to the mag-

In order to evaluate the atomic-level pressure and charge transfer, the calculation was repeated for different volume strains. The relaxed atomic structure for each volume strain was further processed with the Locally Self-Consistent Multiple Scattering (LSMS) method [38,39] to calculate the atomic-level pressure [40]. Once optimized by VASP, in the LSMS method we did not reoptimize the structure. Atomic-level pressure calculations require a definition of atomic volume in a crystal. We used the Voronoi tessellation as implemented in the LSMS method to decompose a supercell into volumes for each atom in the structure. This approach allows full relaxation of the electron density under cell distortions, minimizing the electronic energy of the system under imposed strain. This electronic relaxation is what distinguishes our method from the affine transformation originally introduced by Nielsen and Martin [41,42]. Atomic potentials were approximated as spherically symmetric (ASA). The exchange–correlation energy was treated in the local approximation using the function of von Barth and Hedin [43]. Energy and electron density were then integrated within a Voronoi polyhedron, thus obtaining the atomic-level information for each atom. In particular, the charge transfer was calculated as a difference between the integrated charge in the Voronoi polyhedron and the total charge of an individual atom. The optimized supercell structures were subject to affine deformations, in which the volume of the supercell was changed and atomic energies were calculated using the LSMS method. In general, the atomic-level stress tensor is defined as [44,45]:

$$\sigma_i^{\alpha\beta} = \frac{1}{\Omega_i}\sum_j f_{ij}^{\alpha} r_{ij}^{\beta}$$

where α and β are Cartesian coordinates, Ω_i is the atomic volume at site i, and f_{ij}^{α} and r_{ij}^{β} are the force and distance between atoms i and j. The atomic-level hydrostatic pressure is then given as:

$$p_i = \frac{1}{3}Tr\left(\overline{\overline{\sigma}}_i\right) = \frac{1}{3}\left(\sigma_i^{xx} + \sigma_i^{yy} + \sigma_i^{zz}\right)$$

Under the volume strain we applied to the supercell, the atomic-level pressure can be calculated for each atom as the negative of derivative of the energy with respect to the atomic volume. Accordingly, we calculated the energy of each atom at two different volumes with ± 0.5% volume strain and calculated the derivative by dividing the difference in energy at two different strains by the volume strain. The electron density was integrated within the Voronoi polyhedron associated with each lattice site to calculate the local charge transfer.

3. Results

3.1. Dependence of ELLD on the atomic number: EXAFS experiment

The EXAFS spectrum includes the information about the element-resolved local atomic structure (i.e., the average bond length and the local static fluctuation of bond lengths of each element) of the selected elements in an alloy. In particular, the EXAFS peak height is determined by the number of nearest-neighbor atoms (N_j, where j is the constituent element), the scattering amplitude (f_j), and the EXAFS Debye-Waller factor (σ_j^2), according to the EXAFS equation[46],

$$\chi(k) = \sum_j \frac{N_j f_j(k) e^{-2k^2\sigma_j^2}}{kR_j^2} \sin\left[2kR_j + \delta_j(k)\right] \quad (1)$$

where $\chi(k)$ is the oscillation of the absorption as a function of the photo-excited electron wave number k, R_j is the distance to the neighboring atom, and $\delta_j(k)$ is the phase-shift. The EXAFS Debye-Waller factor reflects the local static fluctuation (standard deviation) of bond lengths, which is also called the mean-squared relative displacement (MSRD). For an equiatomic 3d CCA, assuming a random structure, N_j is $12/n$, where n is the number of constituent elements (the effect of SRO is discussed later) as there are 12 first nearest neighbor atoms in an *fcc* structure. All elements (Cr, Mn, Fe, Co, Ni) have similar f_j values near 0.95 (See Section 2.2). As a consequence, the peak height of the EXAFS spectrum is inversely correlated with the magnitude of σ_j^2.

Fig. 1 shows the Fourier transform profiles $|\chi(R)|$ of the EXAFS spectra of Cr-K, Mn-K, Fe-K, Co-K, and Ni-K edges from 3d CCAs (equiatomic Ni, CoNi, FeNi, MnCoNi, MnFeNi, CrCoNi, FeCoNi, CrMnCoNi, MnFeCoNi, CrFeCoNi, and CrMnFeCoNi alloys) at 30 K. The low temperature (30 K) is chosen to minimize the thermal vibration effects, and hence to measure the fluctuation of bond lengths only from atomic interactions; Okamoto et al. [4] reported that the atomic displacement parameter of CrMnFeCoNi, measured by XRD at 25 K, is 23.5 pm^2, which is close to the DFT-calculated mean-squared atomic displacement (MSAD) at 0 K (25.2 pm^2). Every profile shows the typical *fcc* shape with the first nearest neighbor peak located near 2 Å. The height of the first peak has an overall tendency to decrease in the order of Ni>Co>Fe>Mn>Cr throughout all 3d CCAs. The decrease in the peak height reflects the increase in σ_j^2 (hence, local static fluctuation of bond lengths), which follows the order of Ni<Co<Fe<Mn<Cr.

The Fourier transform profiles of the EXAFS spectra of CrMnFeCoNi at different temperatures (30, 77, 130, 196, and 298 K) are presented in Fig. 2**a**. The order of the peak height (Ni>Co≈Fe>Mn>Cr) does not change at different temperatures. The Debye-Waller factor $\sigma^2(T)$ of all elements in CrMnFeCoNi are plotted in Fig. 2**b**. At higher temperature, the σ^2 values increase due to the increase in thermal vibration, but the overall tendency between the σ^2 values of the constituent elements remains similar in all temperature ranges.

In order to quantitatively discuss the trends, we fitted the first peaks of Ni, CoNi, CrCoNi, FeCoNi, MnFeCoNi, CrFeCoNi, and CrMnFeCoNi at different temperatures using the Einstein formula [46],

$$\sigma^2(T) = \frac{(h/2\pi)^2}{2\mu k_B \theta_E} \coth\left(\frac{\theta_E}{2T}\right) + \sigma_{static}^2 \quad (2)$$

where h is the Plank constant, μ is the reduced mass of two adjacent elements, k_B is the Boltzmann constant, θ_E is the Einstein temperature, and T is the measurement temperature. σ_{static}^2 is the temperature-independent part (so-called static disorder) of σ^2, which represents the local static fluctuation of bond lengths due to the atomic interactions. To reduce the number of variables, we make two assumptions for each element fitting process: (1) the coordination number of each bond type N_j is assumed to be $12/n$ (fully random structure); (2) the bond lengths of the central atom and adjacent atoms are assumed to be the same (e.g. $R_{Cr\text{-}Cr}$=$R_{Cr\text{-}Mn}$=$R_{Cr\text{-}Fe}$=$R_{Cr\text{-}Co}$=$R_{Cr\text{-}Ni}$ for fitting the Cr-edge data), which gives the average bond-length of each element.

Fig. 2**c** presents the fitting result of Cr in CrMnFeCoNi at different temperatures as an introductory example. The value of σ_{static}^2 for Cr is 0.0032±0.0006 Å^2, θ_E is 281±19 K, and the disorder due to zero-point vibration is 0.0032 Å^2 [47]. Fig. 2**d** shows the σ_{static}^2 values of elements in Ni, CoNi, CrCoNi, FeCoNi, MnFeCoNi, CrFeCoNi, and CrMnFeCoNi. The non-zero σ_{static}^2 of Ni is expected to come from the zero-point vibration effect [47]. There is a general trend of the σ_{static}^2 values increasing in the order of Ni<Co<Fe<Mn<Cr. This finding experimentally confirms that the local static fluctuation of bond lengths of each element (hence, ELLD) has a dependency on the atomic number.

netism. Magnetism does not strongly affect the outcome relevant to our analysis, as will be discussed in Section 3.2.3 with the example of CrMnFeCoNi.

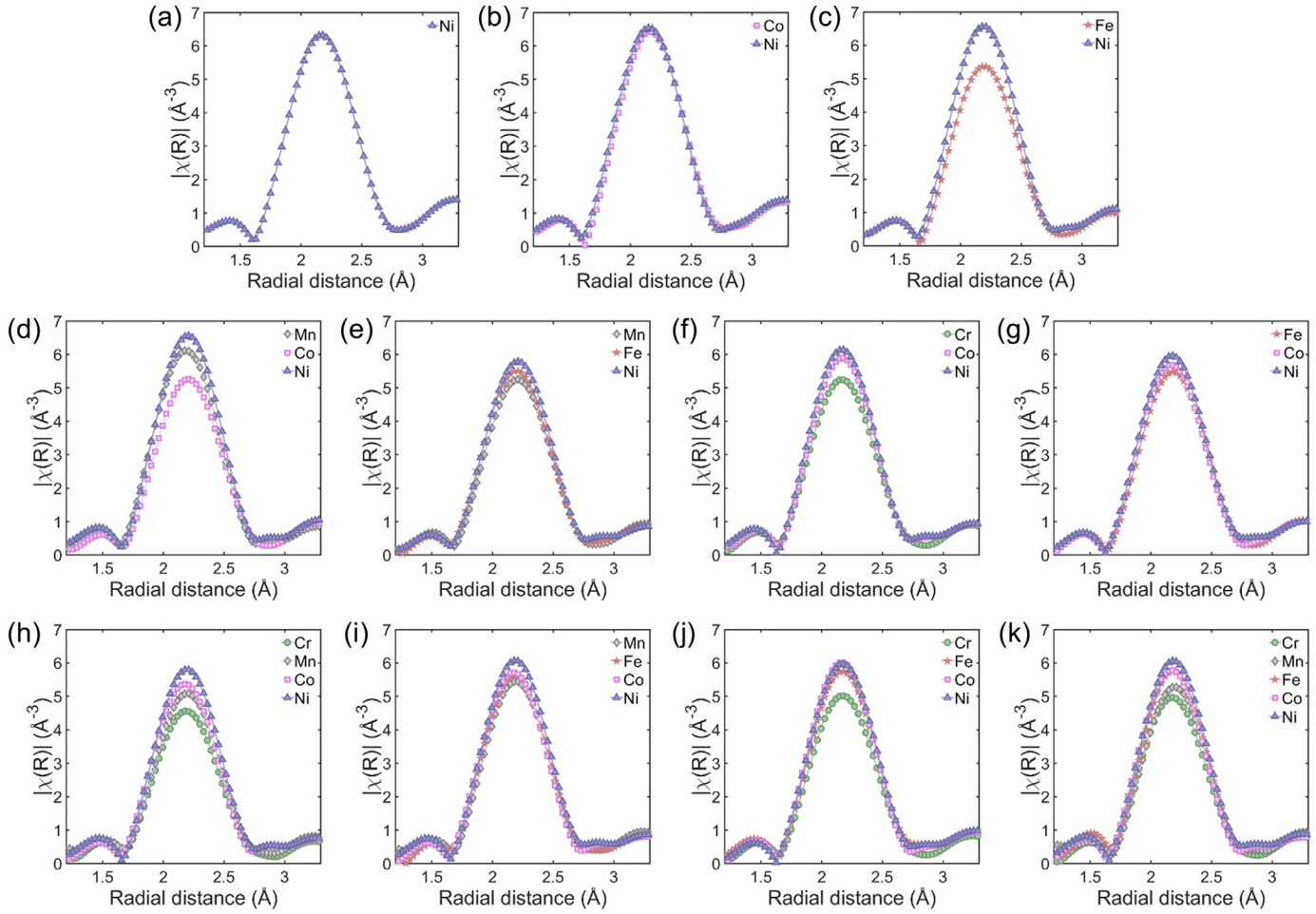

Fig. 1. Fourier transform profiles of the experimental EXAFS spectra at 30 K, showing the dependency of the local static fluctuation of bond lengths on the atomic number in 3d CCAs; Peak heights increase in the order of Cr, Mn, Fe, Co and Ni. (a) Ni, (b) CoNi, (c) FeNi, (d) MnCoNi, (e) MnFeNi, (f) CrCoNi, (g) FeCoNi, (h) CrMnCoNi, (i) MnFeCoNi (j) CrFeCoNi, and (k) CrMnFeCoNi.

3.2. Factors affecting the atomic number dependency of ELLD: DFT calculation

Displacement of an individual atom in CCAs can be affected by various factors, such as atomic size, charge transfer, magnetism, and local ordering. In order to find the origin of the observed dependence between the fluctuation of bond lengths and the atomic number, we perform the DFT calculation that can provide the atom-wise lattice distortion (i.e., atomic displacement) and the quantum-mechanical information of each atom. As a benchmark, CrMnFeCoNi with the ferromagnetic state is chosen (the reason will be explained in Section 3.2.3), and the correlations between the aforementioned factors and ELLD are examined.

3.2.1. Voronoi atomic volume

We first examine the correlation between Voronoi atomic volume and ELLD, as it is an observable topological factor that can partially represent the lattice distortion [20]. Fig. 3**a** presents the DFT-calculated Voronoi atomic volumes and atomic displacements in CrMnFeCoNi. The atomic displacement is calculated as the distance of each atom from the ideal *fcc* crystal sites[2]. The overall trend of the atomic displacement does not have a proportionality with Voronoi-atomic volume. The average Voronoi-atomic volume (the average of the Voronoi-atomic volumes over the atoms of each element) increases in the order of Co (11.49 Å^3)<Fe (11.66 Å^3) ≈Ni (11.66 Å^3) <Cr (11.74 Å^3)<Mn (11.78 Å^3), while the average atomic displacement increases in the order of Ni (0.039 Å)<Co (0.048 Å)<Fe (0.062 Å)<Mn (0.084 Å)<Cr (0.104 Å) (Fig. 3**b**). This correlation can also be seen by the experiment. Fig. 3**c** presents the average bond length of each element (R) and the local static fluctuation of bond lengths of each element (i.e., static disorder) in CrMnFeCoNi measured by EXAFS. The R at 30 K increases in the order of Co (2.514 Å)<Fe (2.524 Å)≈Ni (2.525 Å)<Cr (2.529 Å)<Mn (2.539 Å), while the σ^2 increases in the order of Ni (0.00147 Å^2)<Co (0.00187 Å^2)<Fe (0.00218 Å^2)<Mn (0.00253 Å^2)<Cr (0.00318 Å^2). Thus, the overall trend of the ELLD does not have a proportionality with the average bond length of each element measured by EXAFS.

Similarly, the overall tendency of the atomic displacement of all 3d CCAs in **Fig. S3** correlates with the atomic number rather than the Voronoi-atomic volume. Such a relation between atomic displacement and atomic number was also reported in previous studies[4].Graphical abstract3.2.2.Charge transfer

The electronegativity values of Cr (1.65), Mn (1.75), Fe (1.80), Co (1.84), and Ni (1.88) follow the order of atomic number. Therefore, charge transfer might be the major cause of the observed correlation between atomic number and ELLD. Fig. 4**a** presents the relationship between the atomic displacement and the charge

[2] Atomic displacement is used instead of bond length to resolve the lattice distortion of the individual atom. The change in the bond length before and after the distortion ($d\vec{R}_{ij}$) is the difference between the atomic displacements $\vec{u}_i - \vec{u}_j$ of atoms i and j (**Fig. S2**). Thus, when an atom is easy to displace, the bond length can easily change.

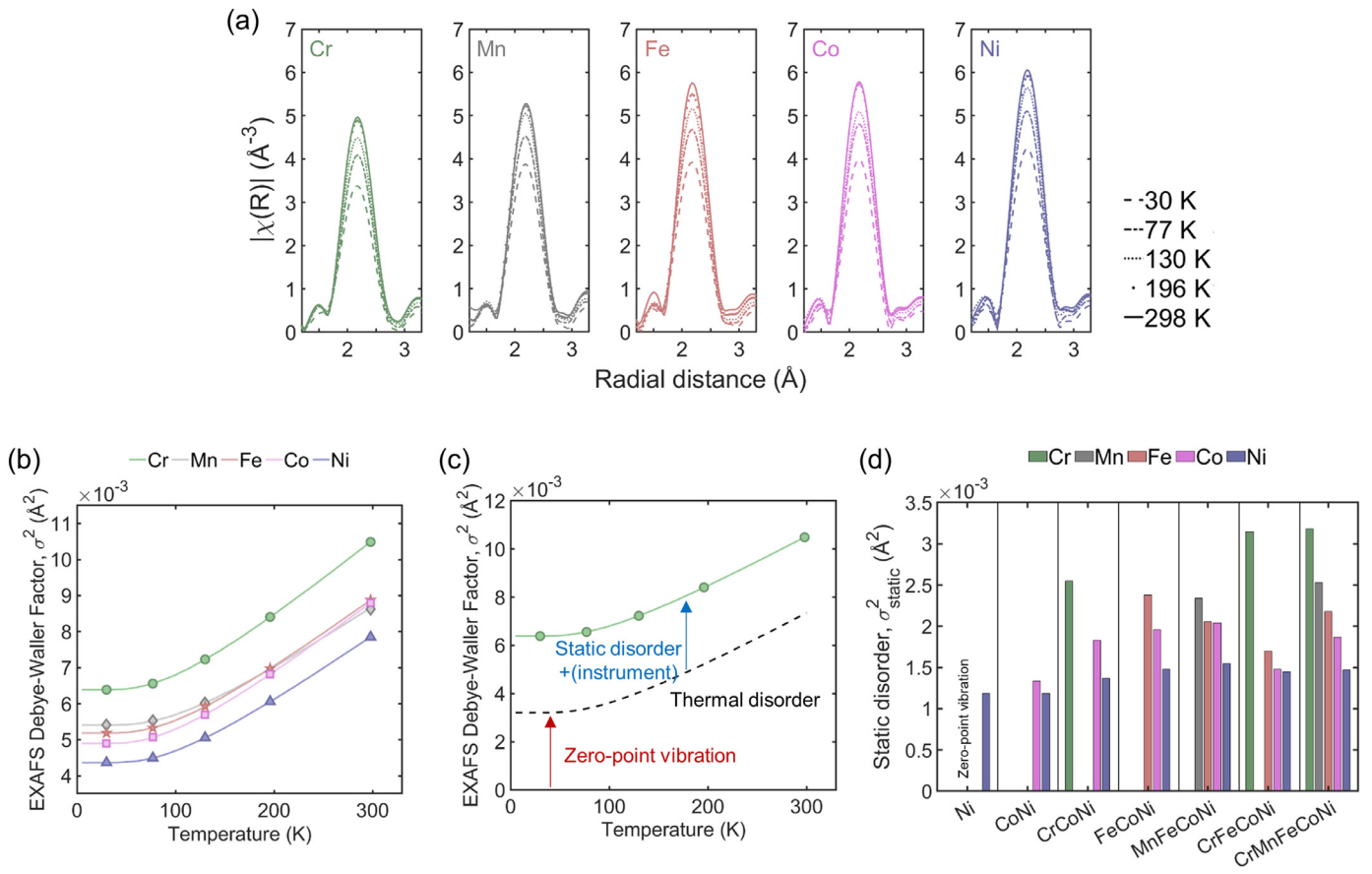

Fig. 2. Dependence of the local static fluctuation of bond lengths on the atomic number in 3d CCAs. (a) Fourier transform profiles of the experimental EXAFS spectra of CrMnFeCoNi at 30, 77, 130, 196, and 298 K. (b) EXAFS Debye-Waller factor of Cr in CrMnFeCoNi and its constituents (static disorder, thermal disorder, zero-point vibration, and instrumental factor). (c) EXAFS Debye-Waller factor of Cr, Mn, Fe, Co, Ni in CrMnFeCoNi at different temperatures, with the fitting lines. (d) Static disorder values of each element in Ni, CoNi, CrCoNi, FeCoNi, MnFeCoNi, CrFeCoNi and CrMnFeCoNi.

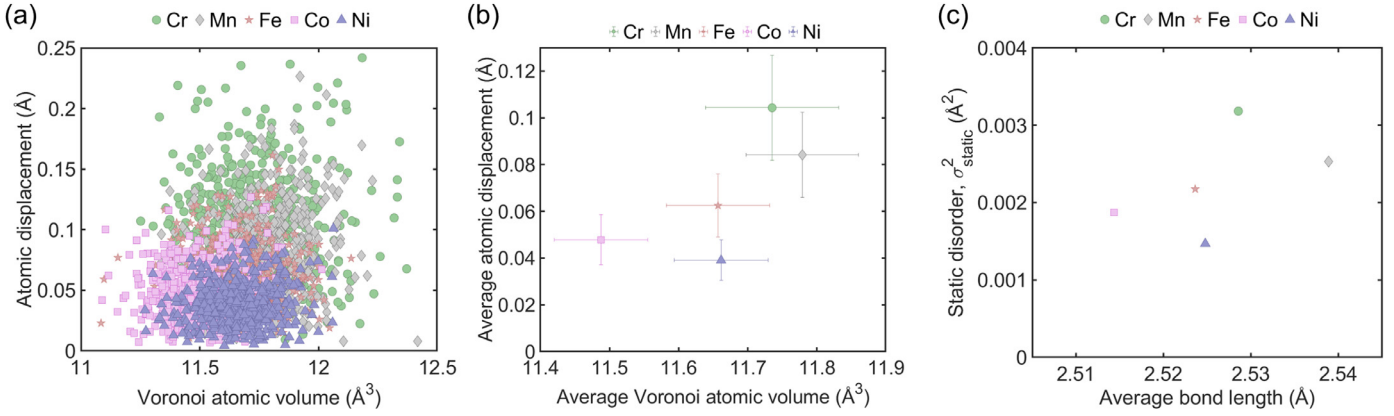

Fig. 3. Effects of (Voronoi) atomic volume in CrMnFeCoNi. (a) Atomic displacement versus Voronoi-atomic-volume relation. (b) Elementwise-average atomic displacement versus elementwise-average Voronoi-atomic-volume, replotted from (a). (c) Static disorder versus average bond length correlation measured by EXAFS.

transfer (Bader charge) of CrMnFeCoNi. Other equiatomic 3d CCAs from the binary CoNi to the quaternary CrFeCoNi are displayed in **Fig. S4**. The overall tendency of atomic displacements follows the charge transfer; elements with negative Bader charges (acquiring electrons) have small atomic displacements and vice versa. Fig. 4**b** presents the relationship between the atomic displacement and the Bader volume. Fig. 4**c** shows the average atomic displacement of each element and fluctuation of atomic displacement of each element due to local static difference shown in Fig. 4**b**, which decrease with an increase in the Bader volume. Assuming random chemical ordering, the degree of the fluctuation of the chemical environment would be similar within all constituent elements in an alloy. The pattern observed through Fig. 4 thus implies that the dependence of the ELLD on the atomic number originates from the chemical character of the central element, which could be the charge transfer (i.e., Bader volume). This tendency is also seen in the experimental results that the static disorder shows a negatively proportional correlation with electronegativity of each element (Fig. 4**d**).

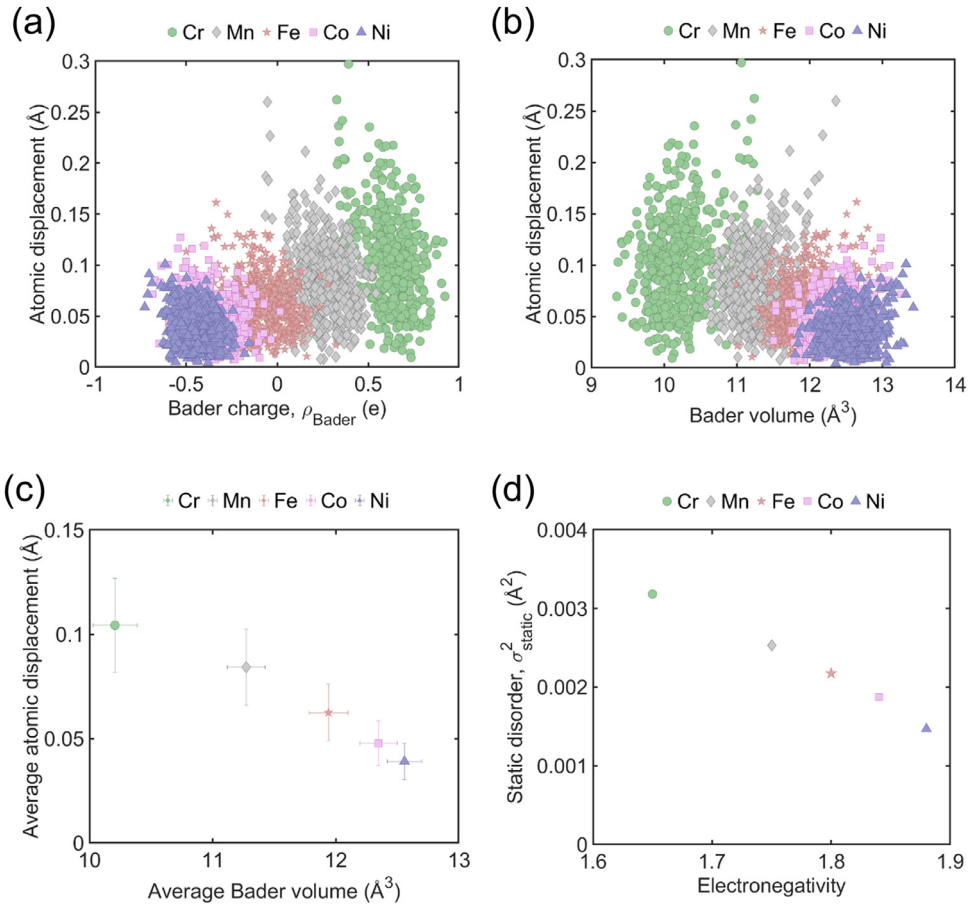

Fig. 4. Effects of charge transfer in CrMnFeCoNi. (a) Atomic displacement versus Bader charge (positive: losing electrons) relation. (b) Atomic displacement versus Bader volume relation. (c) Elementwise-average atomic displacement versus elementwise-average Bader volume, replotted from (b). (c) Static disorder measured by EXAFS versus Electronegativity.

3.2.3. Magnetism

It has been discussed in previous works that the variation in local magnetic moments can affect the lattice distortion in metals [5,48–50]. As 3d CCAs contain either ferromagnetic (Fe, Co, and Ni) or anti-ferromagnetic (Cr and Mn) elements, local spin ordering may affect the ELLD of 3d CCAs. To elaborate on this, we perform the DFT calculations for FM (spin-polarized) and NM (non-spin polarized) states of CrMnFeCoNi to investigate the influence of magnetism on the atomic number dependency of ELLD. Figs. 5**a1** and **a2** present the distribution of magnetic moments of individual atoms in the FM and NM states obtained in this work. Inspecting the converged results, we find for FM state that Fe, Co, and Ni have positive magnetic moments, and Mn has antiparallel magnetic moments to Fe, Co, and Ni. Cr moments converge to both parallel and antiparallel magnetic moments. By construction, in the NM state, all elements have no local magnetic moments.

Figs. 5**b1** and 5**b2** compare the local static fluctuation in bond lengths and average atomic displacement of each element, both of which represent the magnitude of ELLD. The values from EXAFS in Fig. 5**b1** are estimated by $\sigma_{static}/\bar{R}$ ($\bar{R}$: average bond length of each element). Interestingly, the local static fluctuation in bond lengths and the atomic displacements decrease in the order of atomic number (Cr>Mn>Fe>Co>Ni) not only in the FM state but also in the NM state. We therefore conclude that magnetism is not the major origin of the atomic number dependency of ELLD.

However, the observed small impact of magnetism on the atomic dependency of ELLD does not imply the absence of the influence of magnetism on lattice distortion itself. As discussed in a previous work, the agreement between the spin-polarized DFT calculation and the EXAFS experiment for the average bond length of CrMnFeCoNi is completely lost for non-spin polarized (non-magnetic) calculations [5]. Fig. 5**b3** shows the deviation of the average bond length of each element in the FM and NM states. The result from EXAFS at 30 K is also included for comparison. Using the element-wise average bond length R_i (for the i-th element) and the overall average $\bar{R}$, the deviation of the bond length for the i-th element is estimated as $R_i/\bar{R} - 1$. Including magnetism (i.e., FM), the average bond length of each element decreases in the order of Mn≈Cr>Fe≈Ni>Co, which is consistent with the EXAFS result. Without magnetism (i.e., NM), in contrast, the order of the average bond lengths of the elements is substantially modified (Ni>Cr>Co>Mn≈Fe). As stated above, these results were already discussed in a previous work [5] and already indicated a strong coupling between magnetism and local volume of each element. A recent DFT study [50] investigated the effects of magnetism on lattice distortion in various dilute alloys (e.g., 31Cr-1Ni), where the impurity atom in each system was added in the center of the supercell. The study showed that the Bader volume of the impurity atom shrinks in all considered dilute FCC Cr-X alloys (X: Mn, Fe, Co, and Ni), which was explained by the spin fluctuation correlated with the screening behavior of conduction electrons. By enforcing the supercell to have a total initial magnetic moment, the shrinkage is mitigated, and the magnitude of charge transfer decreased to less than half compared to that with the small initial magnetic moment. However, in the present CrMnFeCoNi, neither the shrinkage of average Bader volume nor the change in average Bader charge of

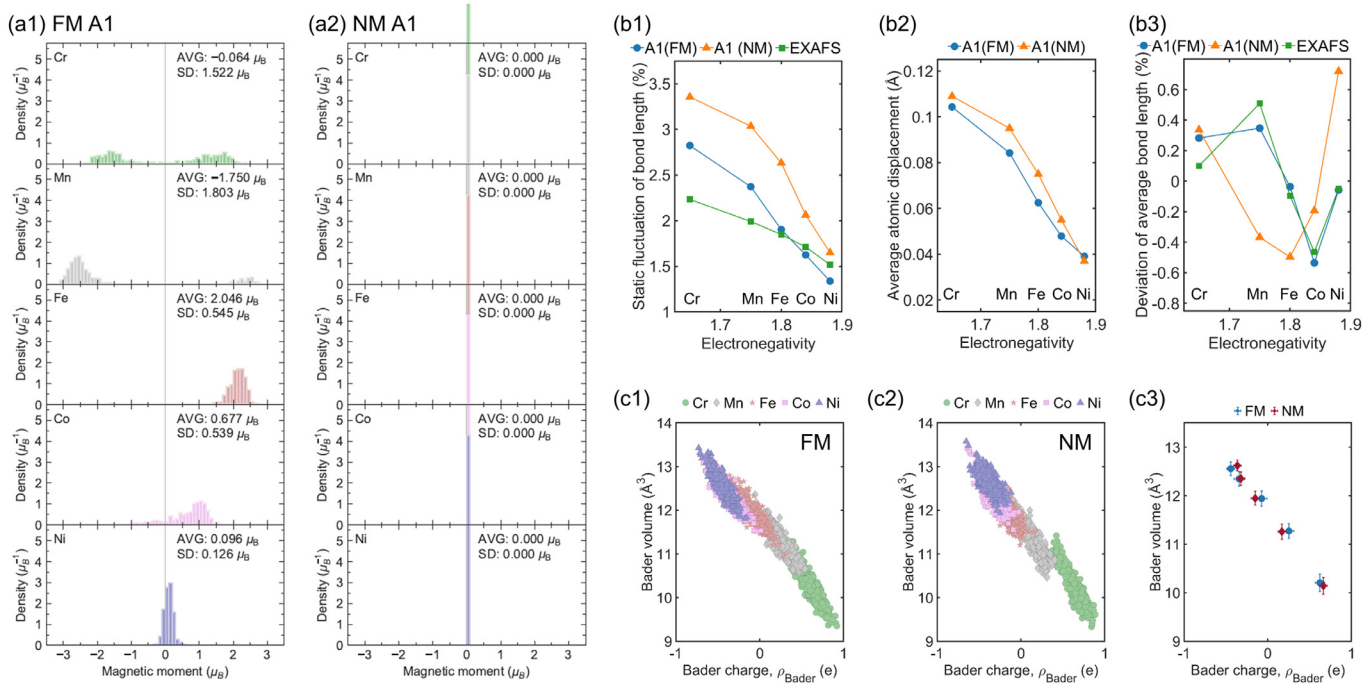

Fig. 5. Effects of magnetism in CrMnFeCoNi. (a) Magnetic moment distribution in (a1) ferromagnetic (FM) fully disordered (A1) structure and in (a2) nonmagnetic A1 structure. (b) Lattice distortion in the FM and NM states; (b1) Static fluctuation of bond length; (b2) Average atomic displacement; and (b3) Deviation of average bond length. (c) Effects of magnetism on charge transfer by comparing Bader volume versus Bader charge in (c1) FM state and (c2) NM state. (c3) Elementwise-average Bader volume versus elementwise-average Bader charge correlations in FM and NM states.

each element is observed when comparing the NM and FM states (Fig. 5**c1–3**). This difference implies the different influence of magnetism in dilute and concentrated alloys, which suggests the danger of extrapolating the results for dilute alloys to CCAs and the importance of considering complex local atomic configurations.

Another important observation is that the absolute sizes of ELLD in the FM state are significantly smaller than those in the NM state. The main effect of magnetism on ELLD is through the magneto-volume effect, because the magnetostriction for 3d elements is small [51]. This explains the volume sensitivity of Cr on magnetism [51]. Further investigations are required to elucidate the decrease of lattice distortion in 3d CCAs in the FM state considering spin fluctuations as well as various local atomic configurations.

In summary, magnetism affects the local atomic volume and decreases the ELLD of each element. However, the atomic number dependency of ELLD persists even in the NM state, implying that magnetism is not the major origin of this dependency.

3.2.4. Short-range ordering

Until now, we have assumed a random configuration of elements, whereas in reality there may be some local chemical ordering as well as local compositional fluctuations. Due to the magnetic spin-ordering, it may be energetically more preferable if the Cr atoms with anti-ferromagnetism are not first-nearest neighbors to avoid magnetic frustration [30]. Indeed the existence of CSRO in CrFeCoNi and CrCoNi has been proposed by simulations (DFT [30]) and experiments (scanning transmission electron microscopy [30,52], EXAFS [53]). Similar Cr-Cr repulsion may be expected also for CrMnFeCoNi, and therefore we also examine the effects of potential Cr SRO on the lattice distortion in CrMnFeCoNi by the DFT calculation. As a hypothetical limit of CSRO, we considered the $L1_2$ phase where Cr only occupies one of the four *fcc* sublattices while the other elements are still randomly distributed (hereafter we call this Cr-$L1_2$), as shown in Fig. 6**a**. Both the fully disordered A1 and the Cr-$L1_2$ phases were modeled based on the SQS concept [24]. The first-nearest-neighbor pair probabilities of the supercell models are summarized in Fig. 6**b**. We also consider both the NM and the FM states to see the impact of magnetism (see details in Section 2.4). The FM states are more stable than the NM states, and the FM Cr-$L1_2$ structure is found to be 2.1 kJ/mol more stable than the FM A1 structure (Fig. 6**c**), which supports the potential SRO in CrMnFeCoNi.

Fig. 6**d1** shows the deviation of the average bond length of each element in the A1 and Cr-$L1_2$ structures in the FM states. The average bond length of each element decreases in the order of Mn>Cr≈Fe≈Ni>Co in both A1 and $L1_2$ structures with the FM states, which is consistent with the EXAFS result (Fig. 6**d**). Cr-sublattice ordering ($L1_2$) does not significantly affect the average bond length except for Cr. Even in Cr, the difference in the deviation of average bond length between the A1 and $L1_2$ structure is only 0.2 % (0.006 Å), which is only ~11 % of the total fluctuation of the bond lengths of the A1 structure (0.053 Å).

Figs. 6**d2 and 6d3** compare the local static fluctuation in bond lengths and average atomic displacement of each element between the A1 and $L1_2$ structures in the FM states. Both the local static fluctuation in bond lengths and the atomic displacements decrease in the order of the element's electronegativity except for Cr in Cr-$L1_2$. In the Cr-$L1_2$ model, Cr occupies only one sub-lattice of the $L1_2$ structure, and inside there are no Cr-Cr bonds—the softest and the most fluctuating bond. The loss of Cr-Cr bonds thus contributes to the smaller ELLD of Cr in the Cr-$L1_2$ model in Figs. 6d2 and 6d3. Thus, local ordering affects ELLD as well as the lattice distortion. However, the partially ordered Cr-$L1_2$ structure is a hypothetical limit of CSRO, and the real alloys have much less CSRO; the real alloys consist of the disordered and the CSRO regions [30,52]. Therefore, the dominant factor for the dependence of the ELLD on atomic number (or electronegativity) is still valid.

Fig. 6**e** compares the Bader charges of the A1 and $L1_2$ structures in the FM states (charge distributions are shown in **Fig. S5**). While the magnitudes of individual charges can depend on the local mag-

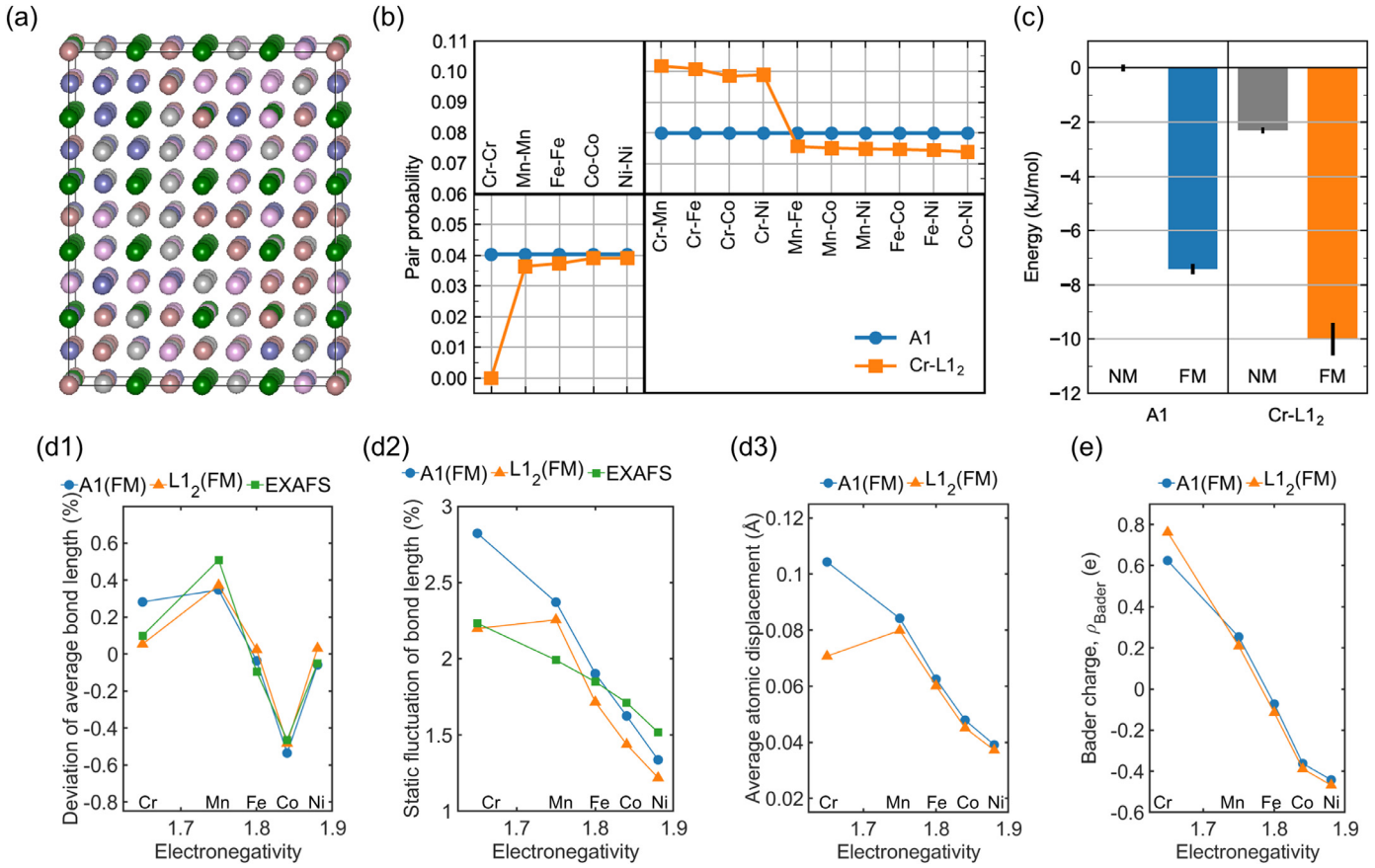

Fig. 6. Effects of short-range order (SRO) on the lattice distortion of CrMnFeCoNi. (a) One of the SRO structure (Cr-sublattice ordering, Cr: Green) used in this calculation. (b) Probability of bond pairs. (c) Comparison of energies between different magnetic states (non-magnetic (NM) and ferromagnetic (FM)) with different structures (A1 and $L1_2$). (d) Lattice distortion in the A1 and $L1_2$ structures; (d1) Deviation of elementwise-average bond length; (d2) Static fluctuation of bond length; and (d3) Elementwise-average atomic displacement. (e) Elementwise-average Bader volume versus elementwise-average Bader charge correlations in A1 and $L1_2$ structures.

netic states and the sublattice orderings, the order of element-resolved averages follows Ni<Co<Fe<Mn<Cr in all the cases. The total difference (standard deviation) in the charge transfer is 0.40 for A1 and 0.44 for $L1_2$; the difference between the two values is about 10 %. This small change implies that the local ordering does not have a significant impact on charge transfer.

4. Discussion

In this study, we show that the ELLD in 3d CCAs follows the atomic number through experiments and DFT calculations. We examine the effects of Voronoi atomic volume, charge transfer, magnetism, and short-range ordering to investigate the origin of the dependence of ELLD on the atomic number. We show that the charge transfer caused by the difference in the electronegativity among the constituent elements dominates the atomic number dependence of ELLD. In this section, we discuss the origin of the correlation between the charge transfer and ELLD and its implication on total lattice distortion. We also discuss the effects of SRO on the solid solution strength in 3d CCAs, which could be drawn from the results of Section 3.2.4.

4.1. Origin of the relationship between ELLD and charge transfer

Previously, some of the present authors showed that the atomic-level pressure in 3d CCAs is dominated by the charge transfer between neighboring elements [14]; an example is shown in the inset of Fig. 7**a**. The elemental dependence thus presents itself also in the relationship between the atomic-level pressure that originates from charge transfer and the atomic displacement (Fig. 7**a** and **Fig. S6**). The atomic-level pressure reflects the gradient of the interatomic potential energies between the central atom and the surrounding environments with respect to volume change. The atomic-level stress $\sigma_i^{\alpha\beta}$ is the first derivative term of interatomic potential energies E with respect to homogeneous (affine) strain, $\varepsilon^{\alpha\beta}$, as:

$$E = E_0 + \varepsilon^{\alpha\beta} \sum_t \Omega_i \sigma_i^{\alpha\beta} \quad (3)$$

where Ω_i is the local-atomic volume [44]. The local energy is strongly affected by charge transfer between the central atom and the surrounding atoms. Thus, the relationship between the atomic displacements and the atomic-level pressure in Fig. 7**a** originates from the dependence of the interatomic potential on charge transfer. When a central atom loses electrons and becomes smaller in size, the central atom and surrounding atoms attract each other to shorten the bond length, and the atomic-level pressure becomes negative. In this case, the interatomic distance between the central atom and surrounding atoms is longer than the minimum position of the atomic pair potential (Fig. 7**b1**). Now, in this case the slope of the potential energy is relatively small reflecting the asymmetry of the interatomic potential. This indicates that atoms with negative (tensile, reduced volume) pressures can be displaced more easily by the effects of local environments. Examples are Cr and Mn in CrMnFeCoNi in Fig. 7**a**. When a central atom obtains electrons and becomes larger, the interatomic distance between a central atom and surrounding atoms becomes shorter than the minimum position of the atomic pair potential (repulsive, Fig. 7**b2**). In this case, the slope of the potential is large, indicating that atoms

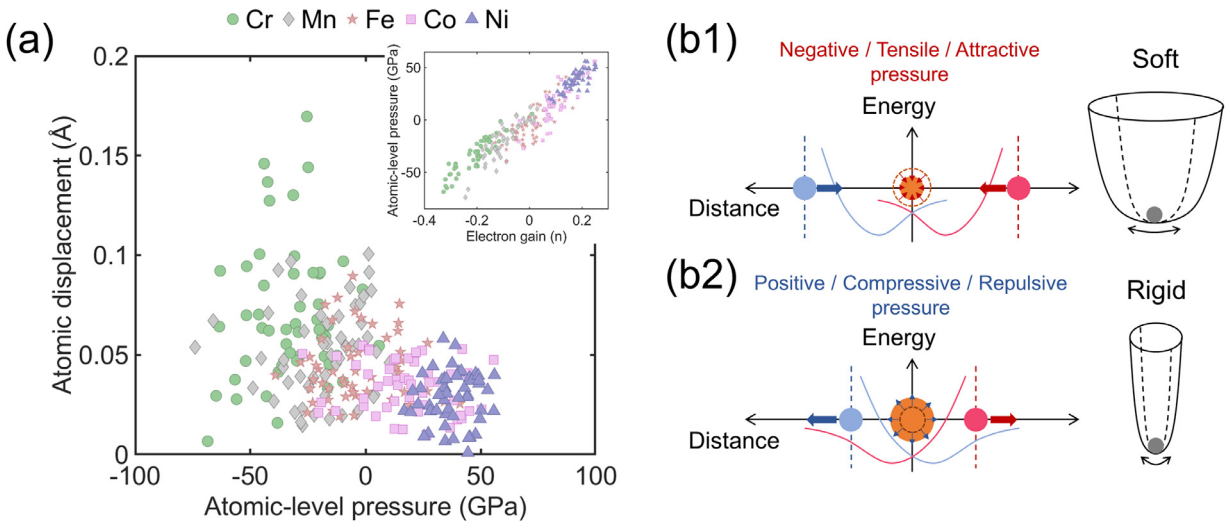

Fig. 7. Dependence of the radial part of the element-resolved local lattice distortion on the charge transfer in CrMnFeCoNi. (a) Atomic displacement versus atomic-level pressure. Inset presents atomic-level pressure versus electron gain. (b) Schematic diagram describing the atomic-level pressure and interatomic potential; (b1) Negative atomic-level pressure (tensile, shrink) with gentle slopes; (b2) Positive atomic-level pressure (compressive, repulsive) with steep slopes. Blue and red circles represent neighboring atoms, and curves indicate the atomic pair potentials with these neighboring atoms.

with positive (compressive) pressures cannot readily be displaced by the effects of local environments. Examples are Co and Ni in CrMnFeCoNi in Fig. 7**a**.

In addition, the intra-atomic charge transfer between different orbitals of the same atom affects the atomic-level pressure, and hence the rigidity of an elemental bonding (the angular component of the lattice distortion) against the environmental fluctuation. The intra-atomic charge transfer and its effects on shear deformation can contribute to the dependence of ELLD on electronegativity. Because of the cubic symmetry of the *fcc* structure, the *d*-electron bands for the e_g orbitals (z^2 and x^2-y^2 orbitals, both extending along [100]) and the t_{2g} orbitals (*xy*, *yz*, and *zx* orbitals, extending along [110]) are different. The ease of intra-atomic charge transfer between the two types of orbitals (i.e., electronic flexibility) results in the ease of atomic displacement which is related to the local shear (angular) distortion. This effect was studied in the migration of interstitial in CCAs by first-principles calculations [54]. During the migration of interstitial, the atoms are angularly displaced from their original lattice sites, forming the saddle state (i.e., the migration barrier). This migration barrier in NiCoCr and NiCoFeCr CCAs is thus dominated by the flexibility of the angular displacement and was shown to be dominated by the ability to transfer electrons from e_g to t_{2g} state. Similarly, the shear component of the local lattice distortion is relaxed by the intera-atomic charge transfer. In addition, in the dislocation core the atomic environment is strongly distorted. The intra-atomic charge transfer will accommodate such local distortions and relax the core structure. We calculate the partial density of state (DOS) of Cr, Mn, Fe, Co, and Ni in CrMnFeCoNi, as shown in Fig. 8**a** and **Fig. S7**. Both e_g and t_{2g} of Ni are nearly filled and the numbers of holes are small (note that the number of holes is equal to the number of states (6 for t_{2g} and 4 for e_g) minus the number of electrons), whereas they are only partially filled for Cr with a large number of holes. Therefore, the charge transfer between the orbitals is easy for Cr, resulting in higher electronic flexibility, whereas Ni is less flexible as schematically described in Fig. 8**b**. Because the filling of the *d*-band depends on the initial number of electrons and the charge transfer, the electronic flexibility decreases with an increase in the atomic number (i.e., electronegativity) in the present case.

As a consequence, both the inter-atomic charge transfer and the intra-atomic charge transfer affect the lattice distortion toward the same direction: the less the number of electrons, the easier to displace atoms and vice versa. Fig. 9 shows the DFT-calculated local static fluctuation of bond lengths of each bond pair normalized by the average bond length over all elements in CrMnFeCoNi [5] and the average electronegativity of the two elements. Allen's scale is used as it reflects Fermi energies of *d* elements [55]. The clear trend of the decreasing fluctuation of bond lengths against the average electronegativity shows that the electronegativity is the signature of the resistance of an element against displacement from its original position. Cr-Cr bonds have the largest fluctuation (3.06 %) and the smallest average electronegativity (1.65). Thus, both Cr atoms can easily be displaced by fluctuations in the local environments. Ni-Ni bonds have the smallest fluctuation (0.89 %) and the largest average electronegativity (1.88). These small fluctuations reflect the strong tendency of Ni to be fixed at its original position. Ni-Cr bonds have medium fluctuation (1.38 %), as well as an intermediate average electronegativity (1.765). Thus, both average electronegativity and ELLD can be used to qualitatively predict the ease of deformation of a particular element in 3d CCAs and to interpret the effects of element on various physical and mechanical prop-

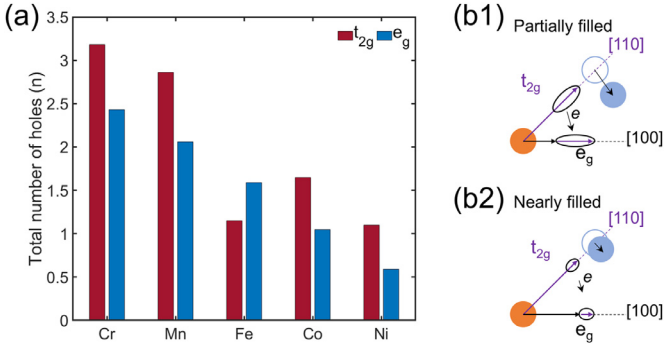

Fig. 8. Dependence of the angular part of the element-resolved local lattice distortion on the charge transfer in CrMnFeCoNi. (a) The total number of holes for t_{2g} and e_g states summed over spins, for Cr, Mn, Fe, Co, and Ni, listed in Supplementary Table 1. (b) Schematic diagram describing the electron transfer between orbitals upon atomic displacement; (b1) Partially filled (e.g. Cr in CrMnFeCoNi); (b2) Nearly filled (e.g. Ni in CrMnFeCoNi).

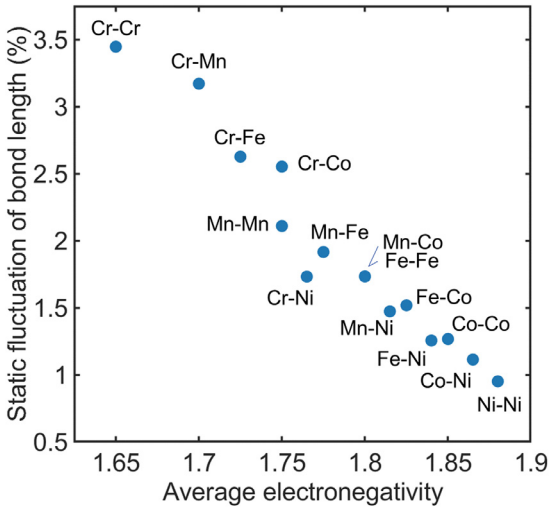

Fig. 9. DFT-calculated local static fluctuation of bond lengths of each bond pair in CrMnFeCoNi[5], plotted against average electronegativity (Allen scale).

erties, whereas in dilute alloys this role is played by the effective atomic size and the size misfit.

4.2. Relationship between charge transfer and total lattice distortion

The dependence of local lattice distortion on chemical elements in 3d CCAs not only explains element-specific problems but also sheds light on the magnitude of the total lattice distortion. Fig. 10**a** displays the atomic displacements of CoNi and CrMnFeCoNi. Both the mean values and fluctuation of atomic displacements of CrMnFeCoNi are larger than those of CoNi. The fluctuation of the charge transfer contributes to the total lattice distortion through two factors. First, the fluctuation in charge transfer is a signature of the fluctuation in the Bader volume and the effective atomic size. The mean size and the fluctuation in the atomic displacements increase with an increase in the fluctuation in charge transfer. Second, the charge transfer includes information about the ease of deformation. The large fluctuation in charge transfer implies that some elements have large negative charge transfers (losing electrons) and are easily displaced. As a consequence, the increase in the fluctuation in charge transfer leads to the increase in the total lattice distortion, which may be the origin of the weak proportional relationship between the electronegativity difference and mean square atomic displacement (MSAD) in 3d CCAs (Fig. 10b). However, note that this statement does not guarantee that the total lattice distortion is solely governed by charge transfer, as additional effects such as magnetism exist [5]. Therefore, further investigation is required to rationalize the traditional proposal of the causality between lattice distortion and complexity-induced properties such as elastic strain energy and solid-solution strengthening.

4.3. Effects of SRO on strengthening in 3d CCAs

The present findings help interpret the effects of SRO on mechanical properties. It has been suggested that SRO has a significant impact on stacking fault energies [56] and various strengthening mechanisms [52,57,58] (i.e., mainly antiphase boundary strengthening, coherency strengthening, and solid-solution strengthening), which together alter dislocation plasticity [56] and complicate the investigation of the role of SRO in the plastic deformation mechanisms. The lesser effects of SRO on charge transfer and total lattice distortion in 3d CCAs (less than 10% with completely ordered Cr-$L1_2$ structure) indicate that the change in the solid-solution strengthening by the formation of SRO may be small (less than 1/10 of the solid-solution strength of a random structure, a few tens MPa) in 3d CCAs. Further, this study considers the partially ordered Cr-$L1_2$ structure as a hypothetical limit of SRO, but real alloys have much less SRO; the small structural changes due to SRO are even more diluted in real 3d CCAs. Indeed, both the standard deviation of the electronegativity values of the constituent elements and the standard deviation of the atomic-level pressure values of the atoms, assuming random configuration, have good proportional relationships with experimentally measured solid-solution strengths in 3d CCAs [14]. Thus, the existence of SRO in 3d CCAs has no significant effect on the solid-solution strengthening due to the low sensitivity of charge transfer to the local structure. In this study, we fix the lattice parameter for the calculation of the Cr-$L1_2$ structure. In reality, however, the lattice parameters of local SRO clusters vary [52], which can generate coherency strengthening effects. Furthermore, low Gibbs energies of SROs can cause diffuse antiphase boundary energies and result in antiphase boundary strengthening [52,57,58]; see Fig. 6**c** as an example. We thus expect that these two mechanisms could be the dominant strengthening mechanisms of SRO in 3d CCAs. Thus, the similarity among ELLD, total lattice distortion, and charge transfer

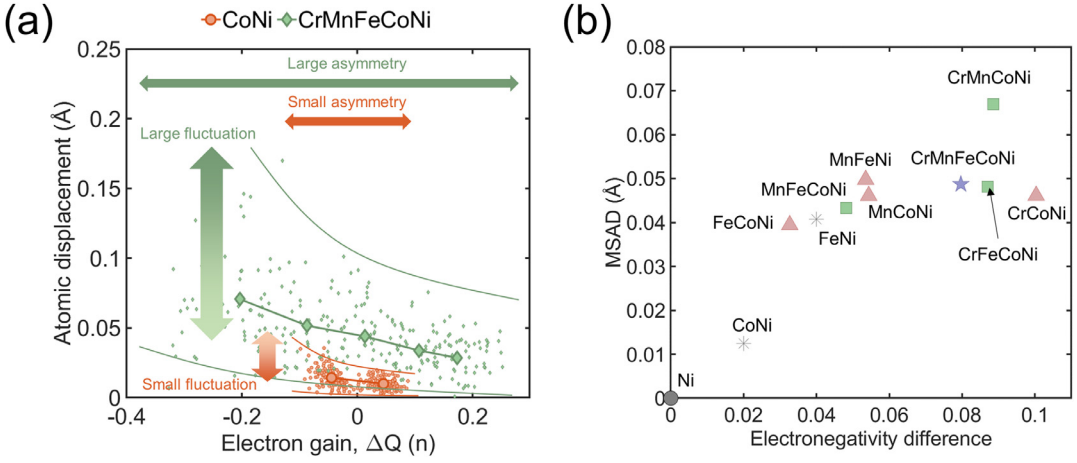

Fig. 10. Relationship among total lattice distortion and charge transfer in 3d CCAs. (a) Atomic displacement and charge transfer (electron gain, negative: losing electrons) of CoNi and CrMnFeCoNi; CrMnFeCoNi shows larger fluctuation in atomic displacements, which indicates complex local atomic environments; more atoms in CrMnFeCoNi have negative electron gain parameters (from -0.1 to -0.4), which results in the large atomic displacements of these atoms. (b) Mean squared atomic displacement (MSAD) of each 3d CCA plotted against the electronegativity difference (standard deviation) among constituent elements.

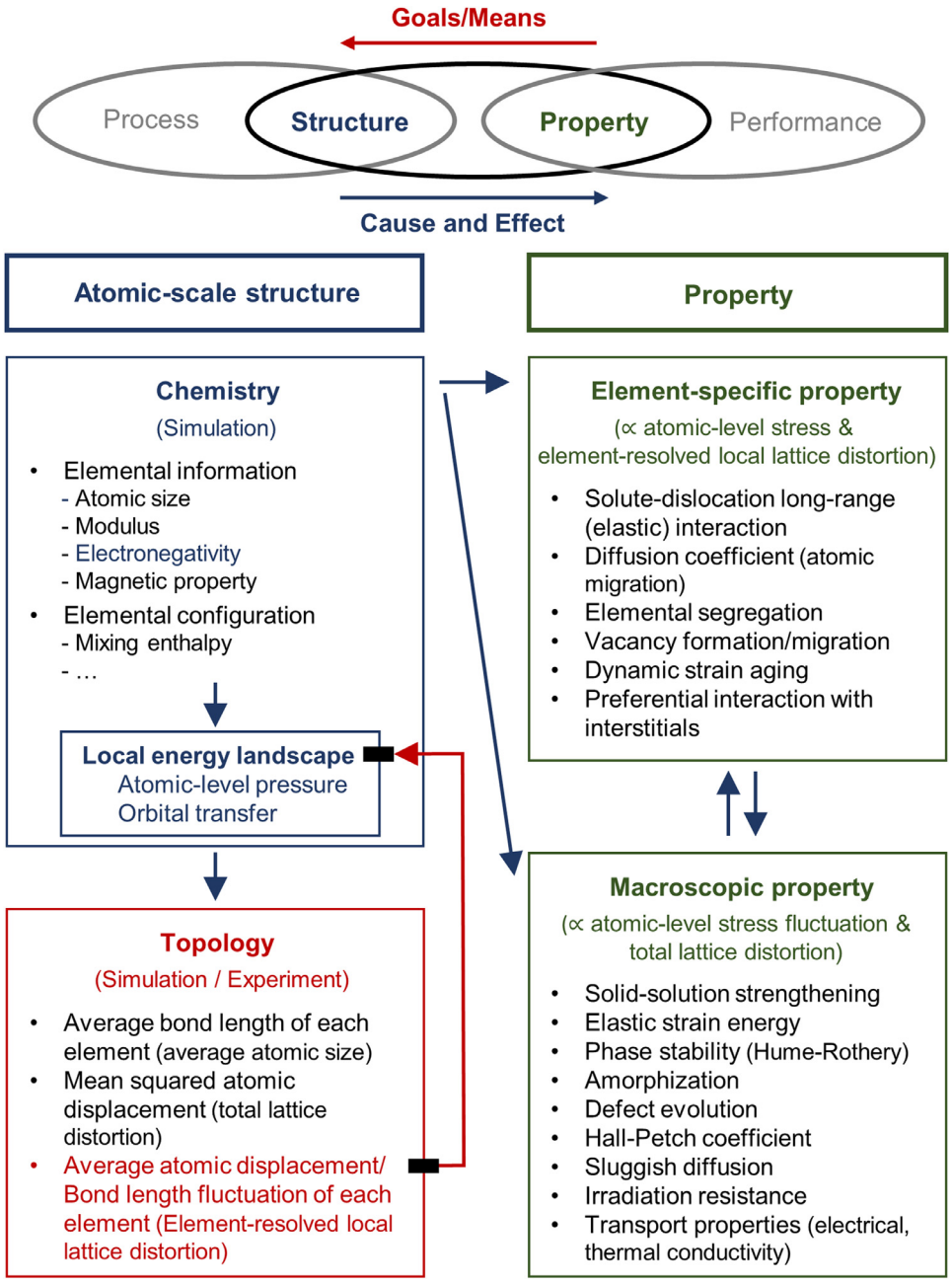

Fig. 11. System chart [61] for atomic-scale design route of CCAs. Only the structure (atomic structure)-property correlation is demonstrated for simplicity. A blue arrow indicates the direction of the cause-and-effect logic of science. A red arrow indicates the direction of the goals-means relations of engineering flow; in addition, once the causality is given, the product (lattice distortion) can be used to infer the cause (local energy landscape) as discussed in this paper.

between A1 and Cr-$L1_2$ structures implies the less effect of SRO on solid-solution strengthening, which reduces the complexity of understanding the impact of SRO on the mechanical behaviors of 3d CCAs.

5. Outlook: Charge transfer, ELLD, and properties of 3d CCAs

The term "lattice distortion" has been often employed to explain interesting properties in CCAs and HEAs. However, the importance of the electronic contributions to both structure and properties has to be recognized when we discuss lattice distortion for such a purpose because the effects of lattice distortion on properties are controlled strongly by the electronic effects in CCAs. In this article, we show that ELLD is an observable signature of charge transfer, and leads to the knowledge of the effective atomic size in 3d CCAs. This new linkage will facilitate understanding how the local structure controls the properties of CCAs, using experimentally observable structural information. Therefore, we suggest re-examining the classical relationship between atomic structure and properties in 3d CCAs based upon the intrinsic atomic size, such as the Goldschmidt radius.

The properties can be divided into two groups (Fig. 11). The first group consists of element-specific properties that can be related to ELLD, such as diffusion coefficient, dynamic strain aging, defect evolution, elemental segregation, and preferential interaction with interstitial solutes. For example, a recent study on tracer diffusion in single-crystalline CrFeCoNi and CrMnFeCoNi shows that the diffusivity of each element at 1373 K increases in the order of Ni<Co<Fe<Cr<Mn [59], which matches the tendencies of the

ELLD and the charge transfer in 3d CCAs in this study. We thus conjecture that the high diffusivities of Cr and Mn in these alloys originate from their low electronegativity values, which result in reduced effective atomic size and hence the easy motion of atoms. In particular, Mn has an abnormally high diffusivity. Considering the low Poisson's ratios in Mn-containing 3d CCAs compared to 3d CCAs without Mn [60], we speculate that Mn has additional effects on the shear stability of the lattice, which calls for further investigations. In addition, Cr or Mn-containing 3d CCAs show serration in their tensile flow above 400 °C [60], which is the signature of the formation of the Cottrell atmosphere around dislocations. Previous studies have discussed the formation of the Cottrell atmosphere based on the diffusivity of elements with small atomic sizes. We speculate that Cr or Mn diffuses fast and form the Cottrell atmosphere near dislocations because of their small effective sizes.

The second group includes the macroscopic properties that have been suggested to be proportional to the total amount of lattice distortion, such as elastic strain energy, phase stability, solid-solution strengthening, sluggish diffusion, electrical conductivity, thermal conductivity, and irradiation resistance. However, as discussed in Section 4.2, it is difficult to correlate the average lattice distortion directly to the fluctuations in charge transfer, thus to the elastic strain energy. Therefore, additional data than the total amount of lattice distortion is required to provide sufficient explanations.

6. Conclusions

In summary, we show that the ELLD in 3d CCAs is highly dependent upon local charge transfer between different elements and between different orbitals of the same atom. The ELLD reflects the degree of atomic displacement upon local environmental fluctuations. Charge transfer affects the ease of radial and axial atomic displacements through inter- and intra-atomic charge transfers. The ELLD is the principal factor that determines the ease of atomic displacement, even though factors other than charge transfer may exist in other types of CCAs, for instance, covalent bonding in Al-containing CCAs. Thus, we suggest that the ELLD can be used as the general qualitative measure of the effective atomic size to predict the contribution of element-specific properties to macroscopic properties of CCAs. Our findings on the correlation among the electronic effects (primarily charge transfer), local energy-related parameters (atomic-level pressure, orbital transfer), atomic structure (ELLD), and related properties will pave the way toward quantitative and well-targeted design of CCAs with improved control of atomic configurations by atomic-level complexity engineering.

Declaration of Competing Interest

The authors declare that they have no known competing financial interests or personal relationships that could have appeared to influence the work reported in this paper.

Data availability

The data that support the findings of this study are available from Prof. Tasan (email: tasan@mit.edu), Prof. Egami (email: egami@utk.edu), Prof. Park (email: espark@snu.ac.kr) upon reasonable request.

Acknowledgements

This work was supported by Creative Materials Discovery Program & Nano•Materials Technology Development Program through the National Research Foundation (NRF) funded by Ministry of Science and ICT, Korea (NRF-2019M3D1A1079215 & NRF-2018M3A7B8060601), U.S. National Science Foundation (NSF) under the grants DMREF-1922206 (MIT) and DMREF-1921987 (UTK)), and by the funding from the German Research Foundation (Deutsche Forschungsgemeinschaft, DFG) within the Priority Programme 2006 (Compositionally Complex Alloys – High Entropy Alloys) and from NWO/STW (VIDI grant 15707). One of the authors (E.S. Park) also benefited from the Center for Iron and Steel Research (RIAM) and Institute of Engineering Research at Seoul National University. Authors thank Dr. Inhui Hwang at Argonne National Laboratory for the assistance of Feff calculations. This research used resources of the Advanced Photon Source, an Office of Science User Facility operated for the U.S. Department of Energy (DOE) Office of Science by Argonne National Laboratory and was supported by the U.S. DOE under Contract No. DE-AC02-06CH11357, and the Canadian Light Source and its funding partners.

Supplementary materials

Supplementary material associated with this article can be found, in the online version, at doi:10.1016/j.actamat.2021.117135.

References

[1] Y. Zhang, Y.J. Zhou, J.P. Lin, G.L. Chen, P.K. Liaw, Solid-solution phase formation rules for multi-component alloys, Adv. Eng. Mater. 10 (2008) 534–538, doi:10.1002/adem.200700240.
[2] J.W. Yeh, S.Y. Chang, Y. Der Hong, S.K. Chen, S.J. Lin, Anomalous decrease in X-ray diffraction intensities of Cu-Ni-Al-Co-Cr-Fe-Si alloy systems with multi-principal elements, Mater. Chem. Phys. 103 (2007) 41–46, doi:10.1016/j.matchemphys.2007.01.003.
[3] S.S. Sohn, A. Kwiatkowski da Silva, Y. Ikeda, F. Körmann, W. Lu, W.S. Choi, B. Gault, D. Ponge, J. Neugebauer, D. Raabe, Ultrastrong Medium-Entropy Single-Phase Alloys Designed via Severe Lattice Distortion, Adv. Mater. 31 (2019) 1–8, doi:10.1002/adma.201807142.
[4] N.L. Okamoto, K. Yuge, K. Tanaka, H. Inui, E.P. George, Atomic displacement in the CrMnFeCoNi high-entropy alloy - A scaling factor to predict solid solution strengthening, AIP Adv 6 (2016), doi:10.1063/1.4971371.
[5] H.S. Oh, D. Ma, G.P. Leyson, B. Grabowski, E.S. Park, F. Kormann, D. Raabe, Lattice distortions in the FeCoNiCrMn high entropy alloy studied by theory and experiment, Entropy 18 (2016) 1–9, doi:10.3390/e18090321.
[6] S.Y. Chang, C.E. Li, Y.C. Huang, H.F. Hsu, J.W. Yeh, S.J. Lin, Structural and thermodynamic factors of suppressed interdiffusion kinetics in multi-component high-entropy materials, Sci. Rep. 4 (2014) 1–8, doi:10.1038/srep04162.
[7] Y. Zhang, G.M. Stocks, K. Jin, C. Lu, H. Bei, B.C. Sales, L. Wang, L.K. Béland, R.E. Stoller, G.D. Samolyuk, M. Caro, A. Caro, W.J. Weber, Influence of chemical disorder on energy dissipation and defect evolution in concentrated solid solution alloys, Nat. Commun. 6 (2015), doi:10.1038/ncomms9736.
[8] S. Mu, S. Wimmer, S. Mankovsky, H. Ebert, G.M. Stocks, Influence of local lattice distortions on electrical transport of refractory high entropy alloys, Scr. Mater. 170 (2019) 189–194, doi:10.1016/j.scriptamat.2019.05.032.
[9] T. Egami, W. Guo, P.D. Rack, T. Nagase, Irradiation resistance of multicomponent alloys, Metall. Mater. Trans. A Phys. Metall. Mater. Sci. 45 (2014) 180–183, doi:10.1007/s11661-013-1994-2.
[10] L.R. Owen, H.Y. Playford, H.J. Stone, M.G. Tucker, Analysis of short-range order in Cu3Au using X-ray pair distribution functions, Acta Mater 125 (2017) 15–26, doi:10.1016/j.actamat.2016.11.048.
[11] Y. Tong, K. Jin, H. Bei, J.Y.P. Ko, D.C. Pagan, Y. Zhang, F.X. Zhang, Local lattice distortion in NiCoCr, FeCoNiCr and FeCoNiCrMn concentrated alloys investigated by synchrotron X-ray diffraction, Mater. Des. 155 (2018) 1–7, doi:10.1016/j.matdes.2018.05.056.
[12] C. Varvenne, A. Luque, W.A. Curtin, Theory of strengthening in fcc high entropy alloys, Acta Mater 118 (2016) 164–176, doi:10.1016/j.actamat.2016.07.040.
[13] S. Yoshida, T. Ikeuchi, T. Bhattacharjee, Y. Bai, A. Shibata, N. Tsuji, Effect of elemental combination on friction stress and Hall-Petch relationship in face-centered cubic high /medium entropy alloys, Acta Mater 171 (2019) 201–215, doi:10.1016/j.actamat.2019.04.017.
[14] H.S. Oh, S.J. Kim, K. Odbadrakh, W.H. Ryu, K.N. Yoon, S. Mu, F. Körmann, Y. Ikeda, C.C. Tasan, D. Raabe, T. Egami, E.S. Park, Engineering atomic-level complexity in high-entropy and complex concentrated alloys, Nat. Commun. 10 (2019) 1–8, doi:10.1038/s41467-019-10012-7.
[15] P. Wang, Y. Wu, J. Liu, H. Wang, Impacts of atomic scale lattice distortion on dislocation activity in high-entropy alloys, Extrem. Mech. Lett. 17 (2017) 38–42, doi:10.1016/j.eml.2017.09.015.
[16] H. Song, F. Tian, Q.M. Hu, L. Vitos, Y. Wang, J. Shen, N. Chen, Local lattice distortion in high-entropy alloys, Phys. Rev. Mater. 1 (2017) 1–8, doi:10.1103/PhysRevMaterials.1.023404.

[17] Q. He, Y. Yang, On lattice distortion in high entropy alloys, Front. Mater. 5 (2018) 1–8, doi:10.1103/PhysRevMaterials.1.023404.

[18] Y. Tong, S. Zhao, H. Bei, T. Egami, Y. Zhang, F. Zhang, Severe local lattice distortion in Zr- and/or Hf-containing refractory multi-principal element alloys, Acta Mater 183 (2020) 172–181, doi:10.1016/j.actamat.2019.11.026.

[19] S. Ishibashi, Y. Ikeda, F. Körmann, B. Grabowski, J. Neugebauer, Correlation analysis of strongly fluctuating atomic volumes, charges, and stresses in body-centered cubic refractory high-entropy alloys, Phys. Rev. Mater. 4 (2020) 1–15, doi:10.1103/physrevmaterials.4.023608.

[20] Y.F. Ye, C.T. Liu, Y. Yang, A geometric model for intrinsic residual strain and phase stability in high entropy alloys, Acta Mater 94 (2015) 152–161, doi:10.1016/j.actamat.2015.04.051.

[21] W.G. Nöhring, W.A. Curtin, Correlation of microdistortions with misfit volumes in High Entropy Alloys, Scr. Mater. 168 (2019) 119–123, doi:10.1016/j.scriptamat.2019.04.012.

[22] B. Ravel, M. Newville, ATHENA, ARTEMIS, HEPHAESTUS: Data analysis for X-ray absorption spectroscopy using IFEFFIT, J. Synchrotron Radiat. 12 (2005) 537–541, doi:10.1107/S0909049505012719.

[23] J.J. Rehr, A.L. Ankudinov, B. Ravel, S.D. Conradson, Real space multiple scattering calculation of XANES, Phys. Rev. B. 58 (1998) 7565.

[24] A. Zunger, S.H. Wei, L.G. Ferreira, J.E. Bernard, Special quasirandom structures, Phys. Rev. Lett. 65 (1990) 353–356, doi:10.1016/j.commatsci.2014.09.021.

[25] P.E. Blöchl, Projector augmented-wave method, Phys. Rev. B. 50 (1994) 17953–17979, doi:10.1103/PhysRevB.50.17953.

[26] G. Kresse, J. Furthmüller, Efficiency of ab-initio total energy calculations for metals and semiconductors using a plane-wave basis set, Comput. Mater. Sci. 6 (1996) 15–50, doi:10.1016/0927-0256(96)00008-0.

[27] G. Kresse, J. Furthmüller, Efficient iterative schemes for ab initio total-energy calculations using a plane-wave basis set, Phys. Rev. B - Condens. Matter Mater. Phys. 54 (1996) 11169–11186, doi:10.1103/PhysRevB.54.11169.

[28] J.P. Perdew, K. Burke, M. Ernzerhof, Generalized gradient approximation made simple, Phys. Rev. Lett. 77 (1996) 3865–3868, doi:10.1103/PhysRevLett.77.3865.

[29] D. Ma, B. Grabowski, F. Körmann, J. Neugebauer, D. Raabe, Ab initio thermodynamics of the CoCrFeMnNi high entropy alloy: Importance of entropy contributions beyond the configurational one, Acta Mater 100 (2015) 90–97.

[30] C. Niu, A.J. Zaddach, A.A. Oni, X. Sang, J.W. Hurt, J.M. Lebeau, C.C. Koch, D.L. Irving, Spin-driven ordering of Cr in the equiatomic high entropy alloy NiFeCrCo, Appl. Phys. Lett. (2015) 106, doi:10.1063/1.4918996.

[31] Y. Ikeda, I. Tanaka, J. Neugebauer, F. Körmann, Impact of interstitial C on phase stability and stacking-fault energy of the CrMnFeCoNi high-entropy alloy, Phys. Rev. Mater. 3 (2019) 68–71, doi:10.1103/PhysRevMaterials.3.113603.

[32] F. Kies, Y. Ikeda, S. Ewald, J.H. Schleifenbaum, B. Hallstedt, F. Körmann, C. Haase, Combined Al and C alloying enables mechanism-oriented design of multi-principal element alloys: Ab initio calculations and experiments, Scr. Mater. 178 (2020) 366–371, doi:10.1016/j.scriptamat.2019.12.004.

[33] Z. Rao, B. Dutta, F. Körmann, D. Ponge, L. Li, J. He, L. Stephenson, L. Schäfer, K. Skokov, O. Gutfleisch, D. Raabe, Z. Li, Unveiling the mechanism of abnormal magnetic behavior of FeNiCoMnCu high-entropy alloys through a joint experimental-theoretical study, Phys. Rev. Mater. 4 (2020) 14402, doi:10.1103/PhysRevMaterials.4.014402.

[34] X. Wu, Z. Li, Z. Rao, Y. Ikeda, B. Dutta, F. Körmann, J. Neugebauer, D. Raabe, Role of magnetic ordering for the design of quinary TWIP-TRIP high entropy alloys, Phys. Rev. Mater. 4 (2020) 1–14, doi:10.1103/PhysRevMaterials.4.033601.

[35] R.F.W. Bader, Atoms in Molecules: A Quantum Theory (International Series of Monographs on Chemistry), Clarendon Press, 1994.

[36] G. Henkelman, A. Arnaldsson, H. Jónsson, A fast and robust algorithm for Bader decomposition of charge density, Comput. Mater. Sci. 36 (2006) 354–360, doi:10.1016/j.commatsci.2005.04.010.

[37] H.J. Monkhorst, J.D. Pack, Special points for Brillouin-zone integrations, Phys. Rev. B. 13 (1976) 5188–5192, doi:10.1103/PhysRevB.16.1748.

[38] Y. Wang, M. Stocks, A. Shelton, Z. Szotek, N. Recently, Order-N Multiple Scattering Approach to Electronic Structure Calculations, Phys. Rev. Lett. 75 (1995) 2867–2870.

[39] W.M. Nicholson, M.C. D., G.M. Stocks, Y. Wang, W.A. Shelton, Z. Szotek, Temmerman, Stationary nature of the density-functional free energy: Application to multiple-scattering accelerated calculations, Phys. Rev. B. 50 (1994) 686–689.

[40] D.M. Nicholson, M. Ojha, T. Egami, First-principles local stress in crystalline and amorphous metals, J. Phys. Condens. Matter. (2013) 25, doi:10.1088/0953-8984/25/43/435505.

[41] O.H. Nielsen, R.M. Martin, First-principles calculation of stress, Phys. Rev. Lett. 50 (1983) 697–700.

[42] D.D. Johnson, D.M. Nicholson, F.J. Pinski, B.L. Gyorffy, G.M. Stocks, Density-functional theory for random alloys: Total energy within the coherent-potential approximation, Phys. Rev. Lett. 56 (1986) 2088–2091, doi:10.1103/PhysRevLett.56.2088.

[43] U. Von Barth, L. Hedin, A local exchange-correlation potential for the spin polarized case. I, J. Phys. C Solid State Phys. 5 (1972) 1629–1642, doi:10.1088/0022-3719/5/13/012.

[44] T. Egami, Atomic level stresses, Prog. Mater. Sci. 56 (2011) 637–653, doi:10.1016/j.pmatsci.2011.01.004.

[45] T. Egami, K. Maeda, V. Vitek, Structural defects in amorphous solids A computer simulation study, Philos. Mag. A Phys. Condens. Matter, Struct. Defects Mech. Prop. 41 (1980) 883–901, doi:10.1080/01418618008243894.

[46] Y. Iwasawa, K. Asakura, M. Tada, XAFS Techniques for Catalysts, Nanomaterials, and Surfaces, 2017, doi:10.1007/978-3-319-43866-5.

[47] W. Bohmer, P. Rabe, Temperature dependence of the mean square relative displacements of nearest-neighbour atoms derived from EXAFS spectra, J. Phys. C Solid State Phys. 12 (1979) 2465–2474, doi:10.1088/0022-3719/12/13/011.

[48] P.M. Marcus, S.L. Qiu, V.L. Moruzzi, The mechanism of antiferromagnetism in chromium, J. Phys. Condens. Matter. 10 (1998) 6541–6552, doi:10.1088/0953-8984/10/29/014.

[49] W.Y. Wang, S.L. Shang, Y. Wang, Y. Jie, K.A. Darling, L.J. Kecskes, S.N. Mathaudhu, X. Dong, Z. Liu, Lattice distortion induced anomalous ferromagnetism and electronic structure in FCC Fe and Fe-TM (TM ¼ Cr, Ni, Ta and Zr) alloys, Mater. Chem. Phys. 162 (2015) 748–756. doi:10.1016/j.matchemphys.2015.06.051.

[50] G. Anand, M. Eisenbach, R. Goodall, C.L. Freeman, Electron spin mediated distortion in metallic systems, Scr. Mater. 185 (2020) 159–164, doi:10.1016/j.scriptamat.2020.04.025.

[51] S. Chikazumi, C.D. Graham, Physics of Ferromagnetism 2e, Oxford University Press on Demand, 2009.

[52] R. Zhang, S. Zhao, J. Ding, Y. Chong, T. Jia, C. Ophus, M. Asta, R.O. Ritchie, A.M. Minor, Short-range order and its impact on the CrCoNi medium-entropy alloy, Nature (2020) 581, doi:10.1038/s41586-020-2275-z.

[53] F.X. Zhang, S. Zhao, K. Jin, H. Xue, G. Velisa, H. Bei, R. Huang, J.Y.P. Ko, D.C. Pagan, J.C. Neuefeind, W.J. Weber, Y. Zhang, Local Structure and Short-Range Order in a NiCoCr Solid Solution Alloy, Phys. Rev. Lett. 118 (2017) 1–6, doi:10.1103/PhysRevLett.118.205501.

[54] S. Zhao, T. Egami, G.M. Stocks, Y. Zhang, Effect of *d* electrons on defect properties in equiatomic NiCoCr and NiCoFeCr concentrated solid solution alloys, Phys. Rev. Mater. 2 (2018) 013602, doi:10.1103/PhysRevMaterials.2.013602.

[55] J.B. Mann, T.L. Meek, E.T. Knight, J.F. Capitani, L.C. Allen, Configuration energies of the d-block elements, J. Am. Chem. Soc. 122 (2000) 5132–5137, doi:10.1021/ja9928677.

[56] J. Ding, Q. Yu, M. Asta, R.O. Ritchie, Tunable stacking fault energies by tailoring local chemical order in CrCoNi medium-entropy alloys, Proc. Natl. Acad. Sci. (2018) 201808660, doi:10.1073/pnas.1808660115.

[57] Q.J. Li, H. Sheng, E. Ma, Strengthening in multi-principal element alloys with local-chemical-order roughened dislocation pathways, Nat. Commun. 10 (2019) 1–11, doi:10.1038/s41467-019-11464-7.

[58] J.B. Cohen, M.E. Fine, Some aspects of short-range order, J. Phys. Radium. 23 (1962) 749–762.

[59] D. Gaertner, J. Kottke, Y. Chumlyakov, F. Hergemöller, G. Wilde, S.V. Divinski, Tracer diffusion in single crystalline CoCrFeNi and CoCrFeMnNi high-entropy alloys: Kinetic hints towards a low-temperature phase instability of the solid-solution? Scr. Mater. 187 (2020) 57–62, doi:10.1016/j.scriptamat.2020.05.060.

[60] Z. Wu, H. Bei, G.M. Pharr, E.P. George, Temperature dependence of the mechanical properties of equiatomic solid solution alloys with face-centered cubic crystal structures, Acta Mater 81 (2014) 428–441, doi:10.1016/j.actamat.2014.08.026.

[61] G.B. Olson, Computational Design of Hierarchically Structured Materials, Science (80-.) 277 (1997) 1237–1242.

[62] B.C. Sales, K. Jin, H. Bei, G.M. Stocks, G.D. Samolyuk, A.F. May, M.A. McGuire, Quantum Critical Behavior in a Concentrated Ternary Solid Solution, Sci. Rep. 6 (2016) 1–8, doi:10.1038/srep26179.